

Supplementary Information

Small modification, Striking Improvement: Super-Fast Charging Over a Wide Temperature Range by Simply Replacing n-propyl Acetate with Isopropyl Acetate

Shengyao Luo,^{‡ab} Mengqi Wu,^{‡b} Said Amzil,^b Tonghui Xu,^b Qing Ming,^b Lei Zhang,^b Jie Gao,^b Shuang Tian,^b Donghai Wang,^c Yisen Qian,^c Ya-Jun Cheng,^{*bc} and Yonggao Xia^{*b}

^a. School of Materials Science and Chemical Engineering, Ningbo University, Ningbo, Zhejiang 315211, China

^b. Ningbo Institute of Materials Technology and Engineering, Chinese Academy of Sciences, 1219 Zhongguan West Rd, Ningbo 315201, Zhejiang Province, P. R. China.

^c. College of Renewable Energy, Hohai University, Changzhou 213000, China.

[‡] These authors contributed equally.

^{*} Corresponding author.

Email: xiayg@nimte.ac.cn, chengyj@nimte.ac.cn.

Supporting Figures

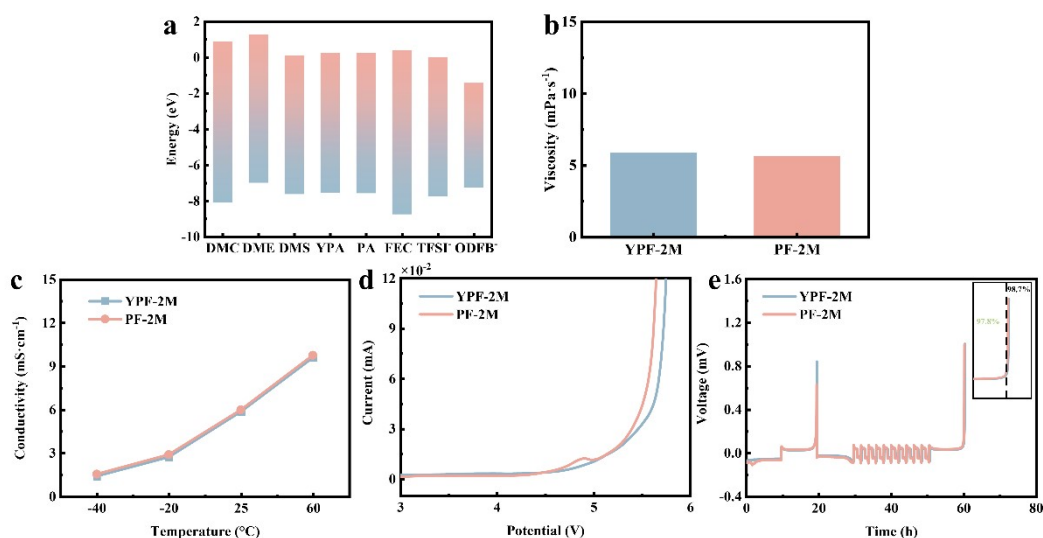


Fig. S1 Calculated HOMO and LUMO energy levels of electrolyte components. (a), viscosity (b), conductivity (c), LSV (d), Li||Cu (e) properties of YPF electrolyte and PF electrolyte of the same component and concentration.

The HOMO-LUMO calculations, viscosity tests, conductivity assessments, Li||Cu cell evaluations, and LSV analyses of YPF and PF electrolytes revealed that their fundamental physical and chemical properties, as well as electrochemical characteristics, were nearly identical.

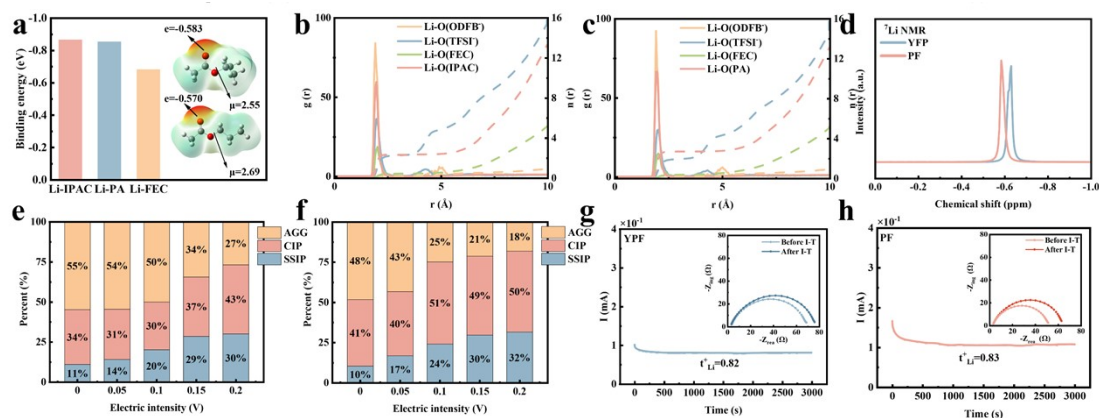


Fig. S2 Li-ion and solvent binding energy (a). RDF curves of YPF and PF electrolyte liquid MD (b, c). The ⁷Li NMR spectrograms of YPF electrolyte and PF electrolyte (d). The proportion and change of ion clusters in YPF and PF electrolytes under different electric field intensities (e, f). Ion migration number test of YPF and PF (g, h).

Calculations of the dipole moment and static charge of the solvent molecules showed that the isopropyl group contributed a more negative charge to the carbonyl oxygen (-0.583) compared to n-propyl while exhibiting a smaller dipole moment (2.55 D) (Fig. S2a). When evaluating the binding energies between lithium ions and carboxylates,¹⁻³ it was observed that the binding energy for Li-IPAC was slightly higher

than for Li-PA, indicating that IPAC can relatively stably occupy the first solvation layer. Additionally, the three-dimensional van der Waals volume of the isopropyl group also occupies this layer.⁴ The weak dipole moment of IPAC renders it less effective at shielding the electric field around lithium ions, thereby expanding the influence radius of the positive electric field, which facilitates the entry of anions into the first solvation layer.^{5,6}

Due to the strong binding affinity, low polarity, and nonlinear spatial volume characteristics of isopropyl acetate, YPF electrolyte exhibits a lower coordination number in radial distribution function (RDF) calculations performed via molecular dynamics (MD), allowing more anions to enter its first solvation layer compared to PF electrolyte (Fig. S2b-c). This observation is further corroborated by NMR measurements, which showed a high-field shift in the ⁷Li peaks (Fig. S2d). A uniform electric field simulation was employed to model liquid phase changes during operational conditions under the influence of an electric field (Fig. S2e-f).^{7, 8} During electric field enhancement, ions driven by this force gradually dissociate into different ion clusters. Among these clusters, AGG (aggregates) refer to ion groups in which multiple ions are closely bound together, while CIP (contact ion pairs) involve a more intimate binding between an ion and its counterion. Notably, YPF consistently maintains a higher proportion of AGG with minimal dissociation occurring between 0 V and 0.1 V. Ion clusters characterized by elevated AGG ratios are generally regarded as favourable for forming inorganic-rich EEI films; however, high levels of CIP preserve ion cluster attributes while also enhancing viscosity, conductivity, and other properties. When comparing SSIP ratios between both electrolytes—despite being nearly equivalent—it becomes challenging to ascertain superiority definitively. Furthermore, the analysis concerning ion cluster structure within liquid phases did not adequately account for interfacial influences nor sufficiently evaluate overall electrolyte quality.⁹⁻¹⁴ Nevertheless, due to both electrolytes' elevated AGG/CIP ratios observed during I-T testing under a pressure differential of 10mV (Fig. S2g-h), both YPF and PF electrolytes exhibit exceptionally high lithium-ion migration numbers, indicating significant potential for rapid charging.

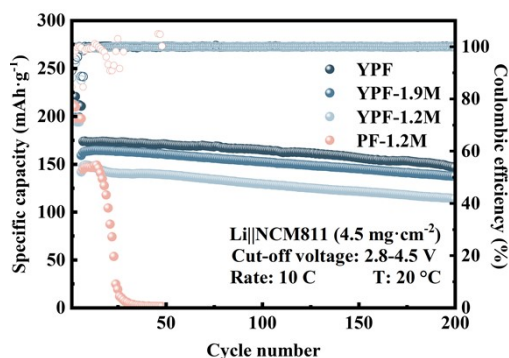


Fig. S3 Cycling curves of Li||NCM811 half-cells in the IPAC system and PA system under different lithium salt concentrations.

The use of an electrolyte with a lower lithium salt concentration can effectively determine the compatibility of the YPF system with low-lithium-salt concentrations. These include **YPF** (1.9M LiTFSI+0.2M LiODFB in IPAC: FEC = 8:2 (v)), **YPF-1.9M** (1.9M

LiTFSI in IPAC: FEC = 8:2 (v)), **YPF-1.2M** (1M LiTFSI+0.2M LiODFB in IPAC: FEC = 8:2 (v)), and **PF-1.2M** (1M LiTFSI+0.2M LiODFB in PA: FEC = 8:2 (v)). When conducting high-rate cycling at 10 C in Li||NCM811 cells, it can be found that the YPF systems all exhibit extremely high stability and capacity performance. Among them, the YPF electrolyte has the highest capacity, while the capacities of YPF-1.9M and YPF-1.2M are lower but their stabilities are similar. From this, it can be judged that neither the LiODFB additive nor a high lithium-salt concentration is a necessary condition for the stable cycling of the IPAC system during high-rate cycling. However, a relatively high lithium-salt concentration and a suitable lithium-salt additive can increase the interfacial lithium-salt concentration in IPAC, significantly reduce polarization, and improve capacity performance.

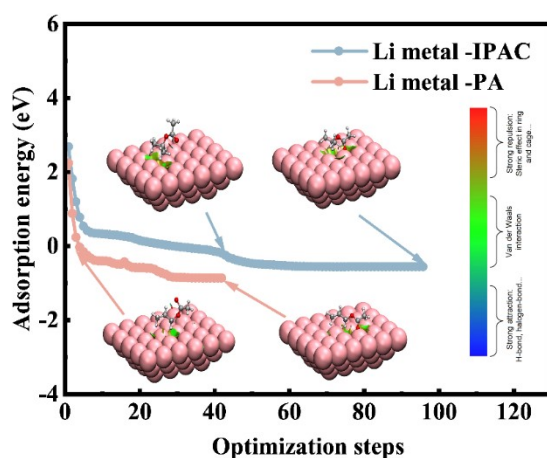


Fig. S4 Adsorption curves of IPAC and PA molecules on the surface of lithium metal.

IPAC solvent molecules have weaker van der Waals force and lower adsorption energy on the surface of lithium metal, and the bond Angle energy barrier connecting isopropyl groups is small during the adsorption process, which makes it easy to escape from the graphite surface.

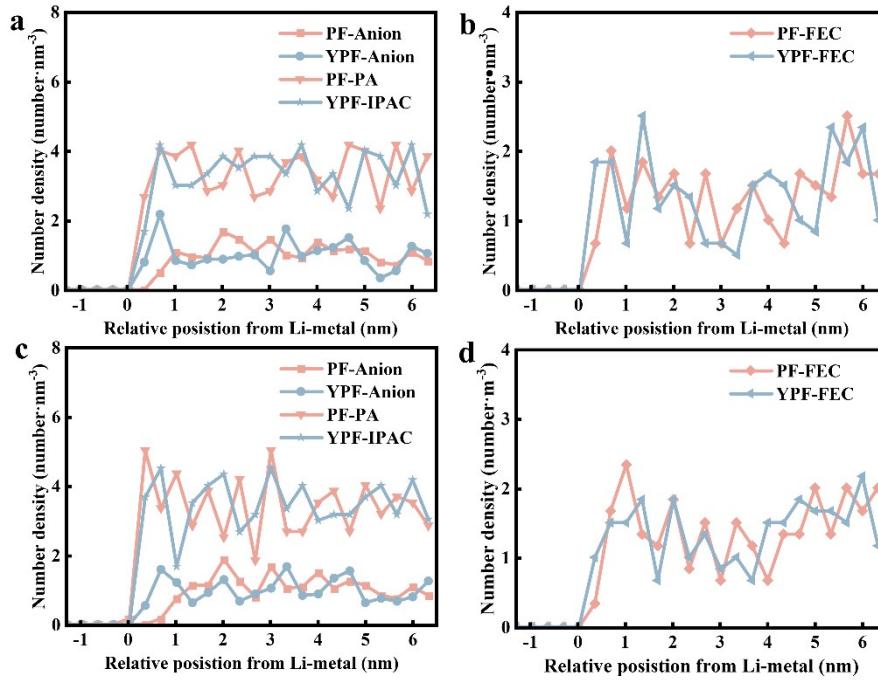


Fig. S5 Molecular adsorption density at the interface (a, b) without electric field and molecular adsorption density at the interface (c, d) with negative charge of lithium metal.

Regardless of whether the electrode surface is charged or not, the anion clusters in the PF electrolyte tend to accumulate at 2nm away from the electrode interface. In the YPF electrolyte, cation and anion clusters are tightly adsorbed at the electrode interface (0.7nm) of the IHP layer. There was little difference in the distribution of FEC molecules.

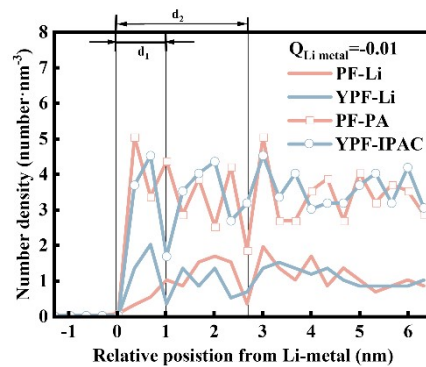


Fig. S6 Adsorption density of lithium-ion and carboxylate molecules at the interface.

The structure of the interface layer is determined by using the carboxylate molecule with the most content and Li^+ which has an opposite charge to the interface. It can be found that the composition difference between the stern layer and diffusion layer of the YPF electrolyte is obvious, while the boundary between the stern layer and diffusion layer of the PF electrolyte is fuzzy.

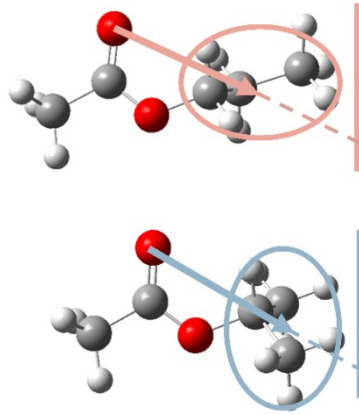


Fig. S7 Defines vectors for PA and IPAC molecules.

The vector is defined as taking carbonyl oxygen as the starting point and the average position of the propyl group as the ending point.

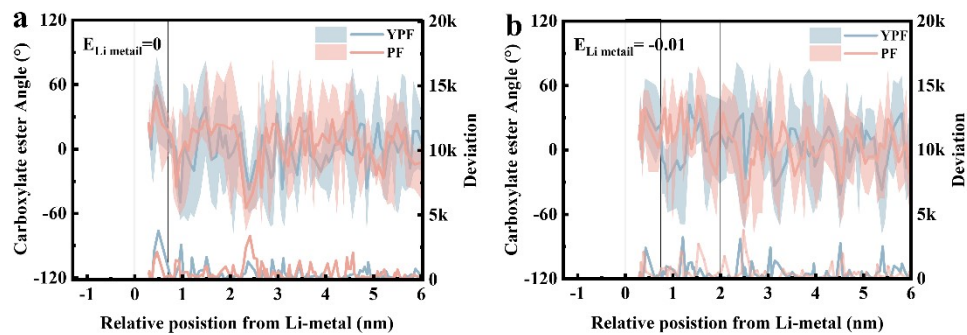


Fig. S8. When the atomic charges are 0 and -0.01 respectively, the average values and distribution of the angles of IPAC and PA molecules (left axis) and the angle deviation values (right axis).

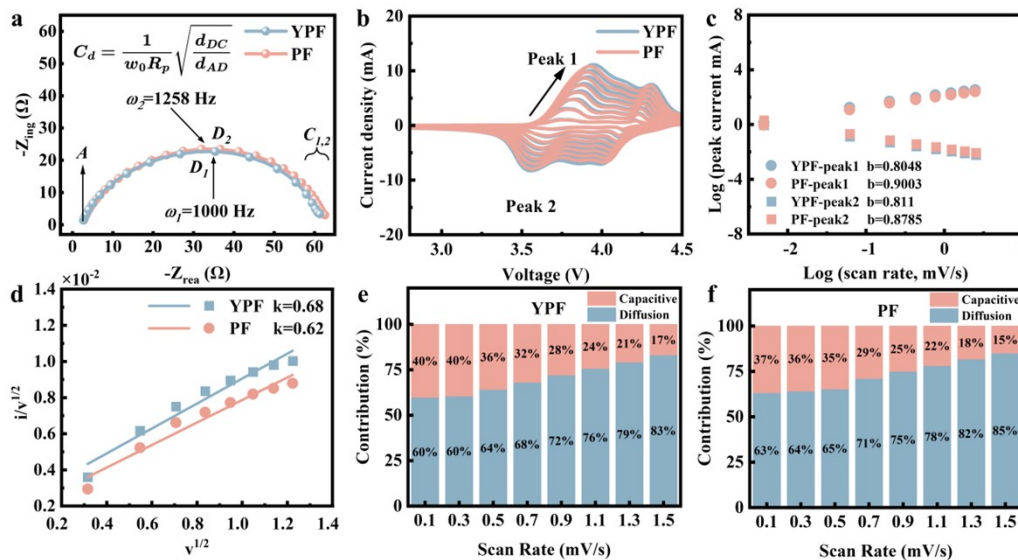


Fig. S9 Complex plane diagram Li||Li Differential capacitance (a) of cells. Cyclic Voltammetry (CV) curve (b) of electrolyte at different scanning speeds in Li||NCM811 cells. The value (c) of electrolyte b (slope) at different peak currents after linear fitting. The k value (d) is to be fitted to calculate the CV capacitance contribution rate in the CV test. Contribution of pseudo capacitance to YPF electrolyte and PF electrolyte at different scanning rates (e, f).

In the Li||Li symmetric cells, the differential capacitance of the YPF electrolyte

($C_d=126.1 \mu\text{F}$) is lower than that of the PF electrolyte ($C_d=152.0 \mu\text{F}$). In addition, in the Li||NCM811 cells, the smaller b value and lower capacitance contribution rate of YPF electrolyte fully indicate that there are more neutral components of YPF electrolyte on the surface of lithium metal, which hinders the double electric layer adsorption of Li^+ on the interface.

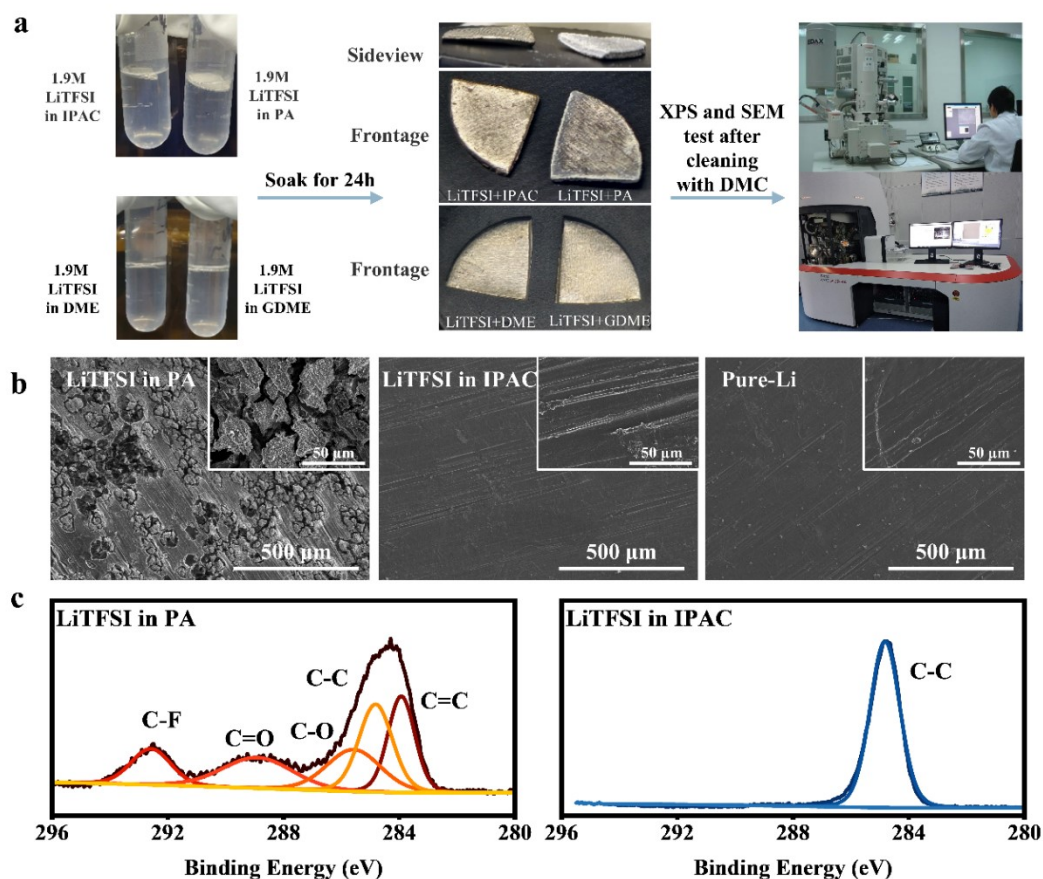


Fig. S10 Flowchart of the immersion experiment for 24 hours: The state diagram of the solution after immersion (a), SEM image of lithium metal after 24 hours of impregnation (b), and the XPS analysis of the immersed lithium metal (c).

a. In the IPAC solution containing lithium salt, even after soaking the lithium sheet for 24 hours, both visual inspection and SEM analysis revealed that the lithium metal surface remained nearly identical to that of a fresh lithium sheet. XPS analysis detected only the C-C component, indicative of conventional contaminant carbon peaks, with no evidence of solution decomposition products.

b. In the n-propyl acetate solution containing salt, significant black-gray decomposition products appeared on the lithium sheet surface after 24 hours of soaking. SEM images showed a large number of loose products distributed across the gray sections of the lithium metal. The XPS carbon profile also revealed substantial solution decomposition products on the lithium metal surface.

c. In the saline ether solvent, the surface smoothness and luster were comparable to those of fresh lithium tablets.

Based on these experimental controls, we can conclude:

1. Comparing control groups b and c, 1.9M LiTFSI is stable relative to lithium metal at room temperature, and the decomposition reaction between lithium metal and the salt-containing PA solvent does not passivate the lithium metal surface.

2. Comparing control groups a and b, the stability of lithium metal in the IPAC solvent containing LiTFSI is significantly greater than in the salt-containing PA solvent, with no detection of solution decomposition components by XPS.

It is evident that despite having very similar electrochemical windows, IPAC and PA exhibit significant differences in their interactions with active lithium metal. Excluding additives, current, and other influencing factors, the enhanced stability of IPAC relative to lithium metal likely stems from differences in the lithium metal interface. This interfacial stability was verified through computational and experimental methods. On one hand, the weak adsorption of isopropyl acetate at the interface and its appropriate orientation reduce contact between carboxylate groups and lithium metal. On the other hand, the higher concentration of lithium ions at the lithium metal interface decreases the proportion of free solvents, thereby enhancing solvent stability.

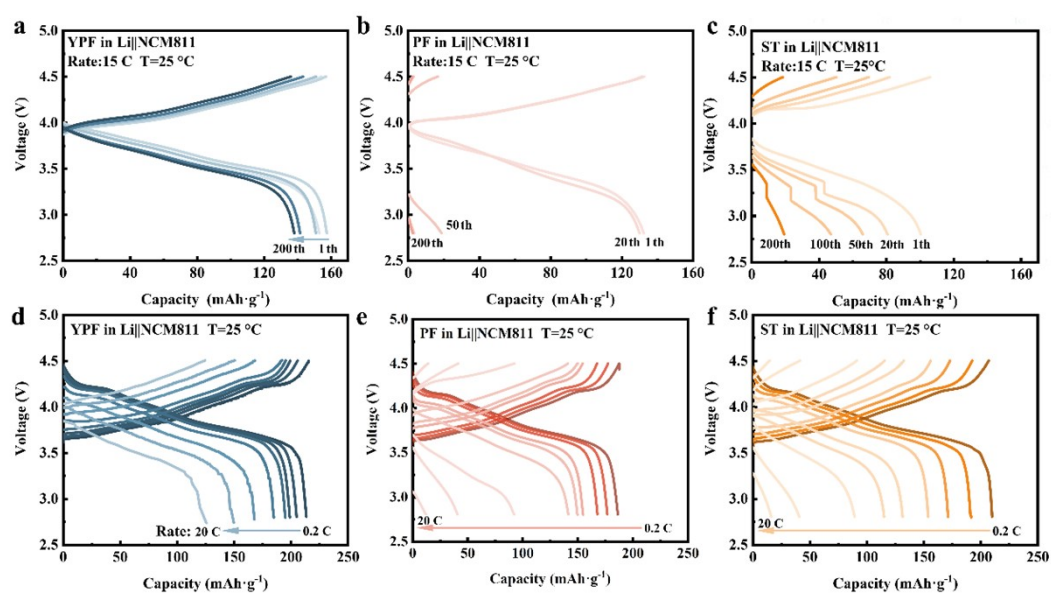


Fig. S11 Discharge curves of the cell with YPF electrolyte under different cycle numbers (a) and at different discharge rates (b). Discharge curves of the cell with PF electrolyte under different cycle numbers (c) and at different discharge rates (d). Discharge curves of the cell with ST electrolyte under different cycle numbers (e) and at different discharge rates (f).

Through the analysis and comparison of the discharge curves of YPF electrolyte with those of PF electrolyte and ST electrolyte, it can be seen that the YPF electrolyte has smaller polarization and more stable capacity. In addition, from the discharge curves, it can be found that the cell degradation trends of PF electrolyte and YPF electrolyte are inconsistent. For the cell with PF electrolyte, in the initial stage of high-rate cycling (<20 cycles), the capacity performance and polarization are similar to those of the YPF electrolyte. However, after 20 cycles, the cell capacity decays rapidly, and the polarization increases rapidly. For the cell with ST electrolyte, the capacity is

low during high-rate cycling, but the polarization trend and capacity attenuation are relatively stable.

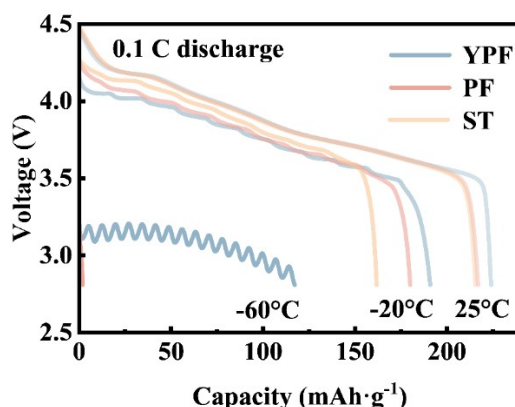


Fig. S12 Discharge curves of batteries with different electrolytes at different temperatures.

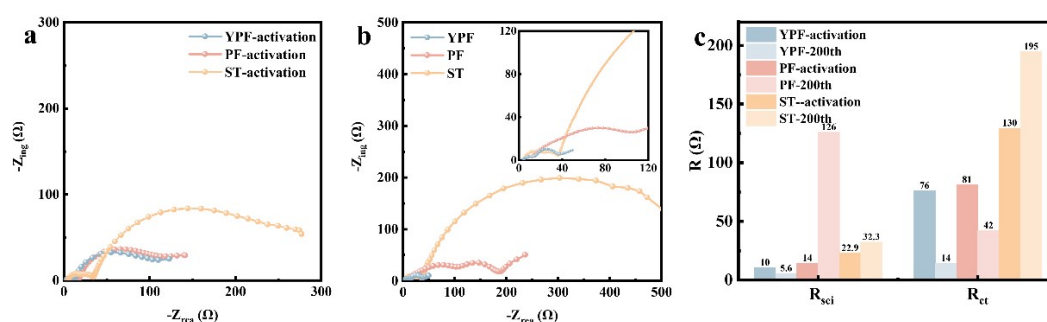


Fig. S13 The EIS of the cells with YPF electrolyte, PF electrolyte and ST electrolyte after activation (a) and the EIS after 200 cycles at a rate of 15 C (b). The R_{se} and R_{ct} were obtained after fitting the EIS with a circuit (c).

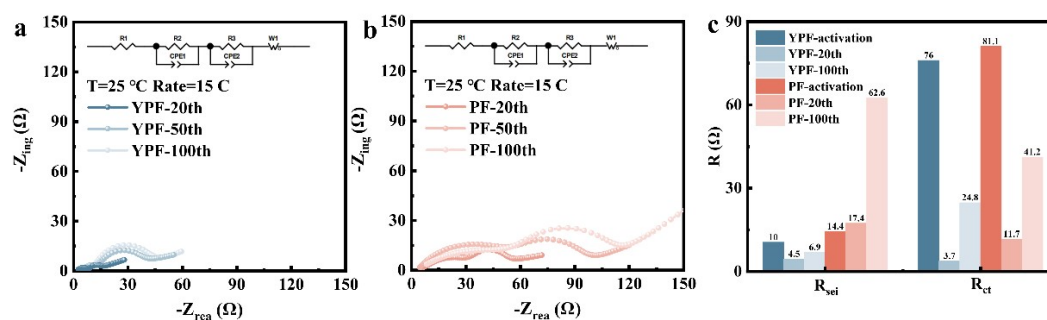


Fig. S14 The EIS curves of Li||NCM811 cells assembled with YPF electrolyte (a) and PF electrolyte (b) at 15 C and 4.5V under different cycle numbers (20th, 50th, 100th). The R_{se} and R_{ct} obtained by fitting the EIS with a circuit (c).

The EIS of Li||NCM811 cells after activation under high voltage and high rate, as well as at the 20th, 50th, and 100th cycles, were analyzed. After fitting, it was found that both YPF- R_{se} and YPF- R_{ct} decreased from the 20th cycle to the 50th cycle, and then increased again when reaching the 100th cycle. This is mainly caused by the decomposition of the electrolyte side reactions to form a film and the reconstruction

of the smooth lithium surface into a lithium surface with a high surface area, which is also a normal part of the cycling process.

In contrast, PF- R_{sei} was slightly larger than YPF- R_{sei} after activation, but it increased rapidly to 53.1 Ω at the 50th cycle during high-rate cycling. The change in R_{sei} is mainly caused by the variation in the impedance of the interfacial film. The interfacial film with rapidly increasing impedance on the electrode surface in the PF electrolyte is one of the consequences of the rapid consumption of the electrolyte.

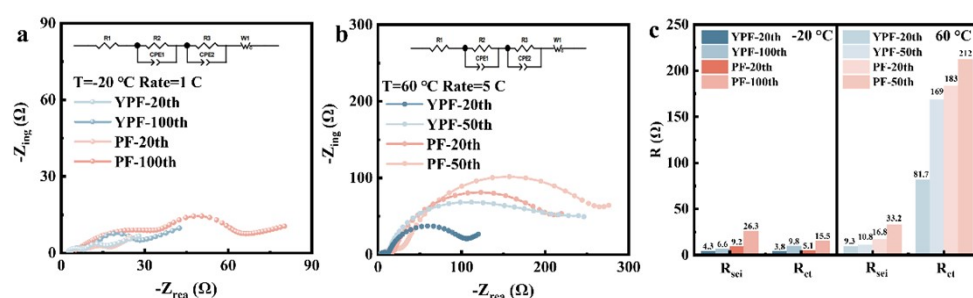


Fig. S15 The EIS curves of Li|NCM811 cells assembled with YPF electrolyte and PF electrolyte at different cycle numbers during cycling at $-20\text{ }^{\circ}\text{C}$ (a) and $60\text{ }^{\circ}\text{C}$ (b). The R_{sei} and R_{ct} obtained by fitting the EIS with a circuit (c).

At $-20\text{ }^{\circ}\text{C}$, during the cycling of the cell with YPF electrolyte, the values of R_{sei} and R_{ct} are relatively small and increase slowly. For the cell with PF electrolyte, because its impedance is similar to that of the YPF electrolyte after activation, the impedance is low when it reaches the 20th cycle (with a specific capacity of about $120\text{ mAh}\cdot\text{cm}^{-2}$). However, as the number of cycles increases, R_{sei} rises rapidly while the increase in R_{ct} is relatively slow.

At $60\text{ }^{\circ}\text{C}$, the degree of side reactions in the cell is significantly intensified. The values of R_{sei} and R_{ct} of the electrolyte are notably higher than those during room-temperature cycling with the same number of cycles. Among them, the impedance of the PF electrolyte increases rapidly during the cycling process, which is significantly higher than that of the YPF electrolyte.

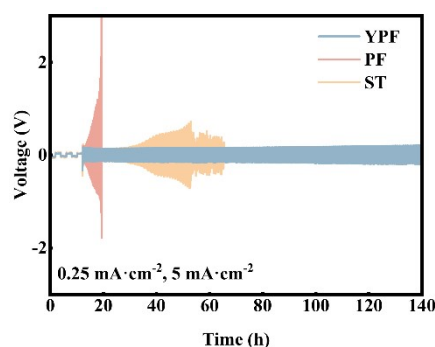


Fig. S16 The cycling curves of Li|Li symmetric cells with YPF, PF and ST electrolytes.

When the Li|Li symmetric cell using PF electrolyte switches to high-current cycling ($5\text{ mA}\cdot\text{cm}^{-2}$), the polarization continuously increases. When charging at the 20th cycle, the polarization voltage reaches above 3 V, and the cell is terminated by the testing equipment. Considering the relatively high conductivity and ionic

transference number of the PF electrolyte, for the Li||Li cell with PF electrolyte, the main reason is that intense lithium dendrites and continuously thickening dead lithium penetrate the separator, resulting in a short circuit of the cell.

During low-current cycling ($0.25 \text{ mA}\cdot\text{cm}^{-2}$) of the cell with ST electrolyte, the cell polarization is greater than that of the PF electrolyte and YPF electrolyte. When switching to high-current cycling, the voltage polarization is similar to that of the YPF electrolyte within 50 cycles. After more than 50 cycles, the cell polarization intensifies, and a short circuit occurs at the 160th cycle. This is mainly because after the EC, which easily reacts with lithium metal in the ST electrolyte, is gradually consumed, DMC decomposes to generate an unstable high-impedance interface, accelerating the consumption of electrolyte components and generating more lithium dendrites, which ultimately penetrate the separator and cause a short circuit.

The YPF electrolyte maintains an extremely low and stable polarization during both low-current and high-current cycling, indicating that the electrolyte plays an excellent role in suppressing side reactions of lithium metal and the formation of lithium dendrites.

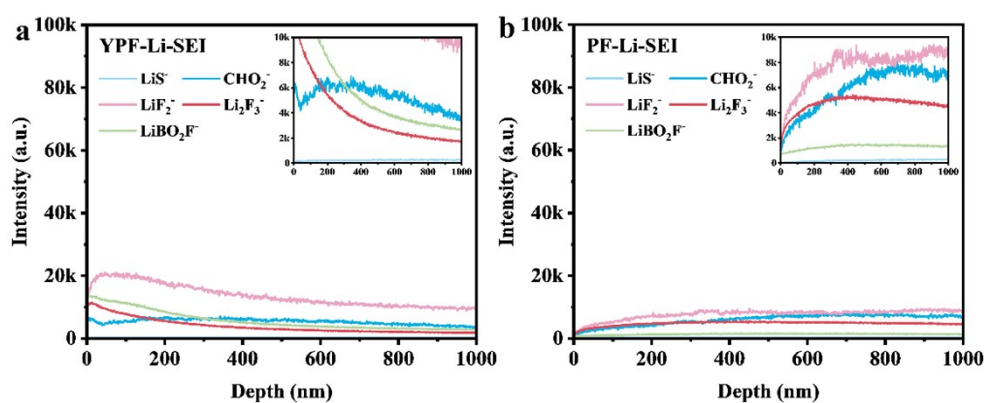


Fig. S17 Ion depth curve obtained by TOF-SIMS test on lithium metal side after different electrolyte cycling.

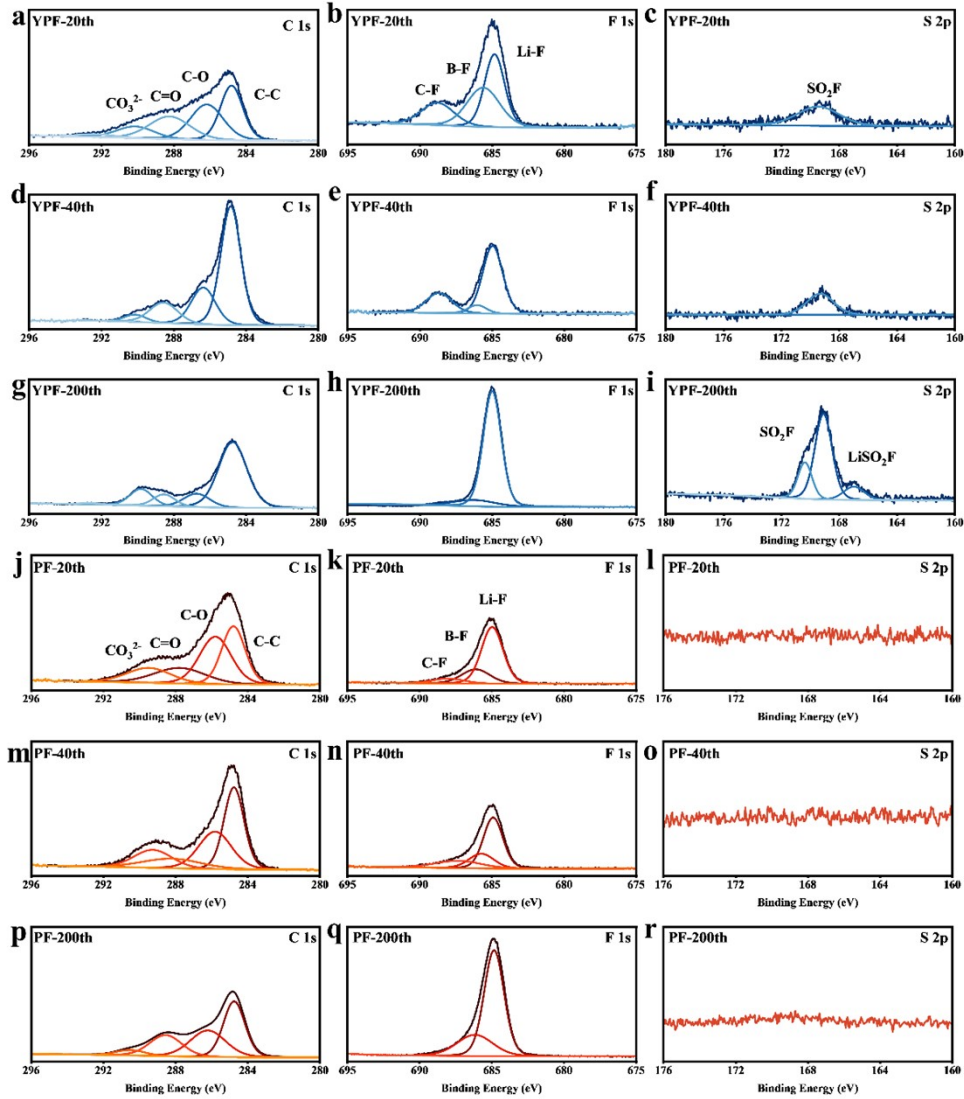


Fig. S18 XPS analysis of the lithium-metal end after different electrolytes are cycled at 15 C for 20, 40, and 200 cycles: YPF electrolyte (a-i), PF electrolyte (j-r).

For the Li||NCM811 cell with YPF electrolyte, at the 20th cycle, the SEI layer contains certain amounts of products such as C-F, Li-F, B-F, and SO_2F , which mainly come from the decomposition of the lithium salt. As the cycling progresses, LiF dominates at the lithium-metal, and CO_3^{2-} and SO_2F products continuously accumulate during the cycling process.

For the cell with PF electrolyte, the LiF content is relatively high at the 20th cycle, corresponding to a relatively high specific capacity (about $130 \text{ mAh}\cdot\text{cm}^{-2}$) in the cycling performance. As the cycling continues, the S element is never detected. Since LiTFSI is the main lithium salt in the PF electrolyte, the fact that LiTFSI does not decompose relative to the solvent or decomposes incompletely implies that a large amount of organic components decompose and the lithium-metal end is difficult to passivate under high-rate conditions. The Li||NCM811 cell with PF electrolyte has very few effective cycles after the 40th cycle. Therefore, the main components of the SEI film at the 40th cycle are very similar to those at the 200th cycle.

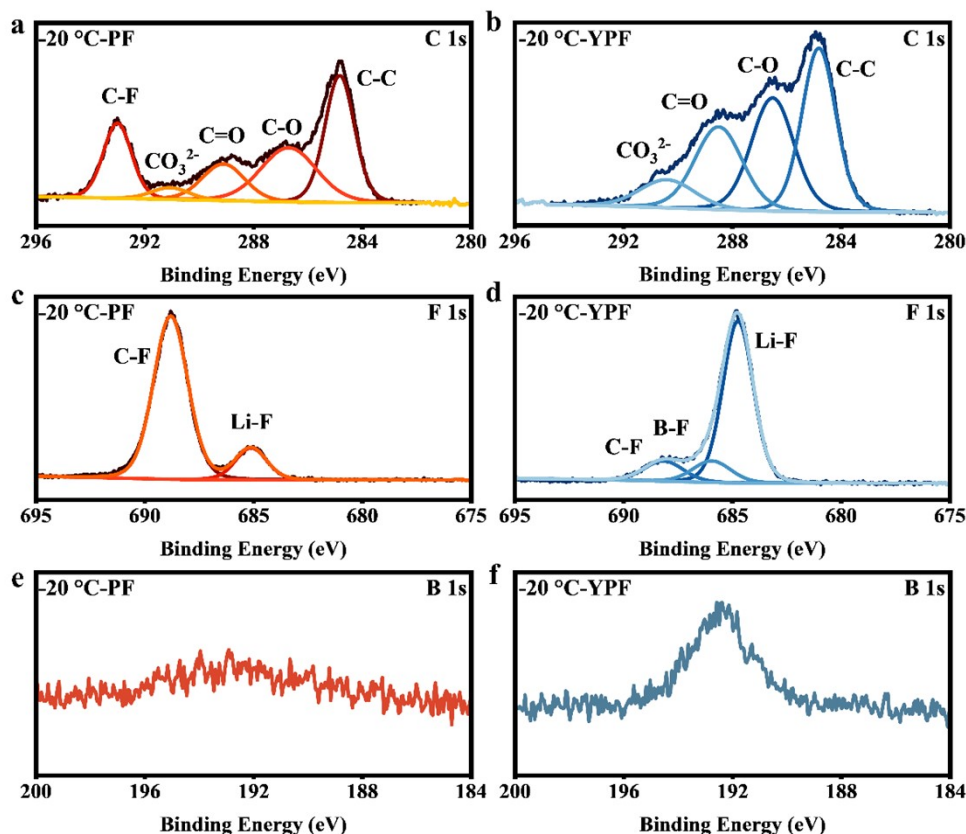


Fig. S19 XPS analysis of the surface of lithium metal in Li||NCM811 cells after 200 cycles at -20 °C and 1 C with different electrolytes: for PF electrolyte, the results are shown in (a), (c), and (e); for YPF electrolyte, the results are presented in (b), (d), and (f).

At -20 °C, the side reactions of the electrodes are relatively weak, and the difficulty of the lithium-salt decomposition reaction increases. Moreover, at a relatively high cycling rate of 1 C, the conductivity of the electrolyte and the interfacial impedance have a greater impact on the cycling stability of the cell. In addition, compared with room temperature, the higher difficulty of uniform lithium deposition leads to the formation of dendrites at the lithium-metal and the occurrence of short-circuit problems.

Compared with the YPF electrolyte, the PF electrolyte does not have sufficient lithium-salt decomposition in preference, resulting in extremely high C-F and Li-F components (mainly from FEC) at the lithium-metal interface. This high-impedance and unstable organic SEI film is extremely vulnerable to being punctured by lithium dendrites. The continuously exposed fresh lithium - metal surface will further increase the interfacial impedance and the risk of the lithium dendrites puncturing the separator. After the FEC component is gradually consumed, the PF electrolyte ultimately has difficulty maintaining a high and stable cycling capacity at low temperatures.

In the cell with the YPF electrolyte, the easily reducible LiODFB decomposes to form an SEI film. Due to the relatively high inorganic components such as LiF and BF, the deterioration of the SEI layer is effectively inhibited.

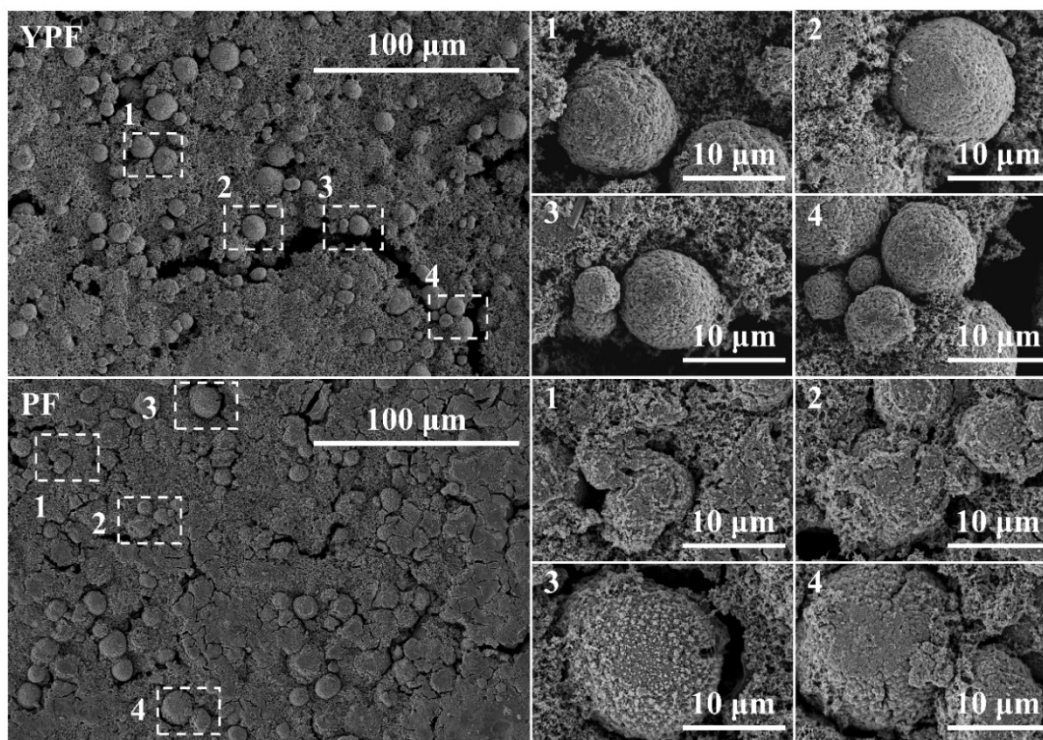


Fig. S20 SEM images of larger areas of NCM811 after cycling at 20 °C and 15 C in different electrolytes.

We conducted a meticulous statistical analysis of particle cracking. Specifically, three SEM images with larger areas were randomly selected. After carefully excluding particles bearing obvious indentation marks, a remarkable finding emerged: the particle cracking ratio in the case of the YPF electrolyte, which is approximately 4%, is substantially lower than that of the PF electrolyte, which is around 13%.

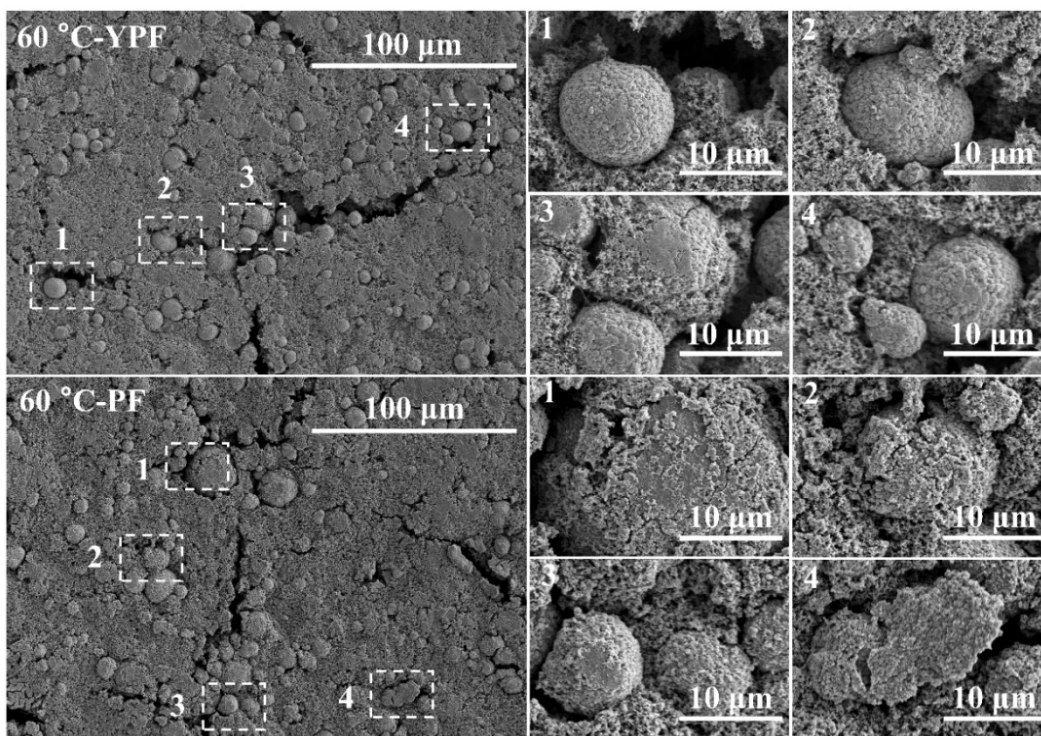


Fig. S21 SEM images of a relatively large area of NCM811 after it has been cycled at 60 °C and 5 C in different electrolytes.

The surface decomposition of NCM811 is significantly intensified at high temperatures. After cycling in YPF electrolyte, the surface smoothness of NCM811 particles (Fig. S20) remains similar to that observed at normal temperatures. However, after cycling in PF electrolyte, the surfaces of NCM811 particles are extensively covered by a substantial amount of insoluble paste, making it difficult to discern the condition of some particles. These pastes, which are insoluble in DMC solution, originate from the extensive decomposition of PF electrolyte at high temperatures. This phenomenon also accounts for the significant capacity fade of PF at elevated temperatures.

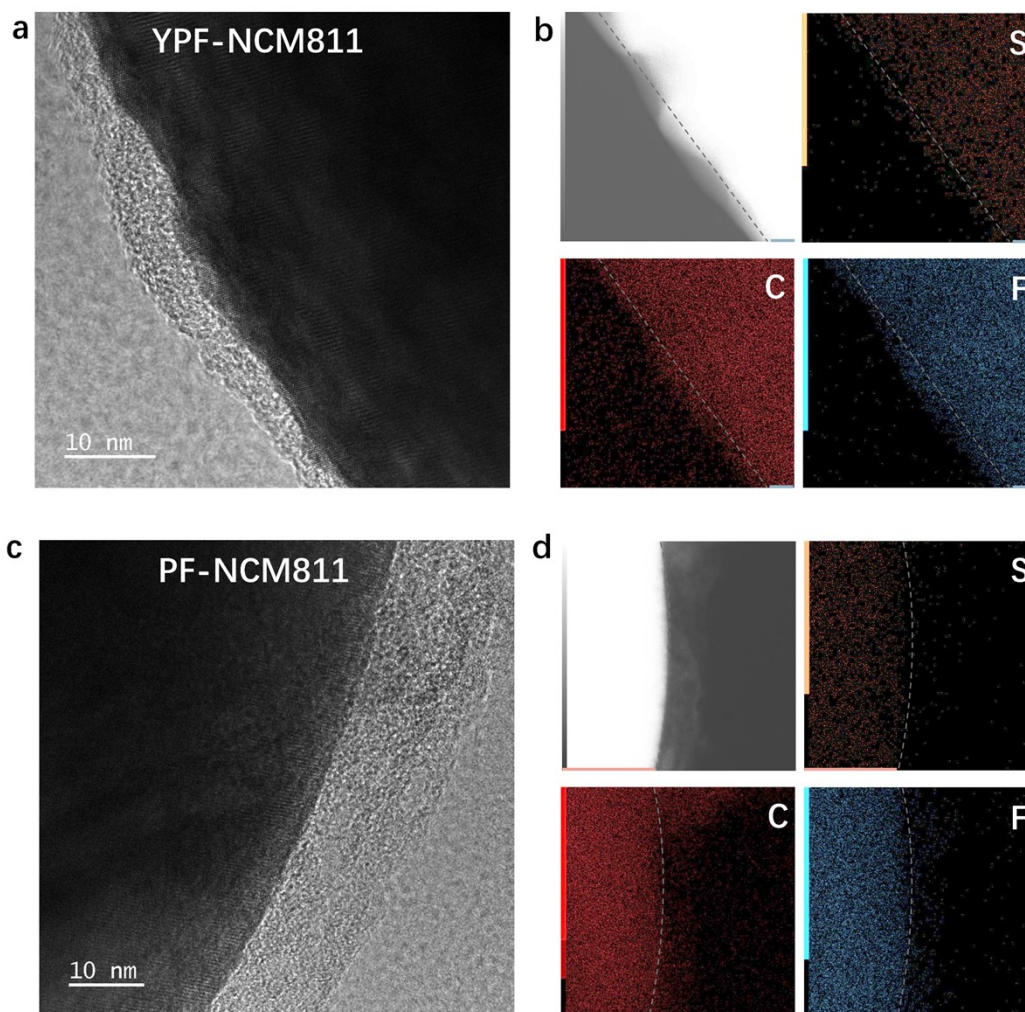


Fig. S22 Images captured by a cold field emission scanning electron microscope and the distribution maps of various elements of NCM811 particles in Li||NCM811 cells after 500 cycles at 10 C with different electrolytes (YPF: a, b. PF: c, d).

The JEM-F200 cold field gun is used to test the disordered surface layer of NCM811 with weaker electron beam energy, which can improve the damage of the disordered surface layer by electron beam energy. After 500 cycles, the disordered surface layer thickness pattern is similar to that of 200 cycles, and the disordered surface layer in YPF electrolyte (about 6.9nm) is still thinner than that of PF (about 16.7nm). This thicker disordered surface layer makes it easier to observe the elemental composition of the disordered surface layer in TEM. In NCM811 cycled with YPF electrolyte, the distribution of C, F, and S elements on the disordered surface layer can be clearly observed. However, in NCM811 cycled with PF electrolyte, only C and F elements are distributed in the disordered surface layer. Due to the interference of C and F elements from PVDF, the S element is direct evidence of the decomposition of LiTFSI into a film at the positive electrode end. (Since the B element is relatively light and has a low content, it is difficult to detect in the small-scale TEM mapping.)

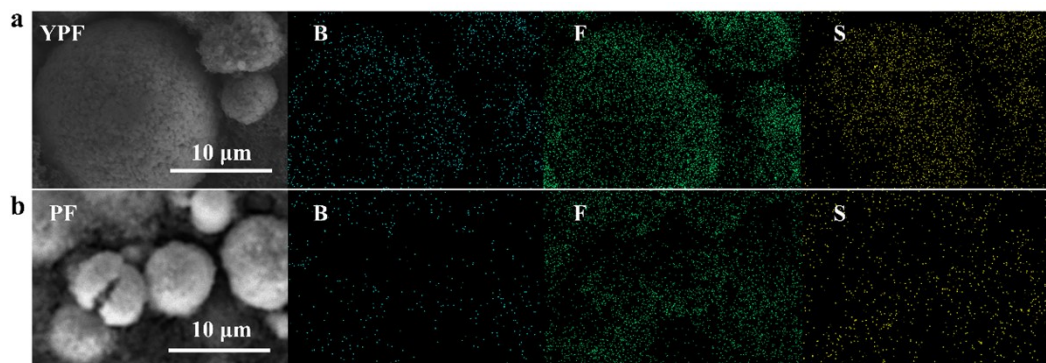


Fig. S23 Images taken by a cold field emission SEM and the mappings of S, C, and F elements (a, b) of NCM811 particles after 200 cycles with YPF and PF electrolytes.

The elemental mapping images of the SEM images of the NCM811 electrode can be mutually verified with those of the TEM. The S element on the surface of the NCM811 particles after cycling in the YPF electrolyte clearly outlines the shape of the NCM811 particles.

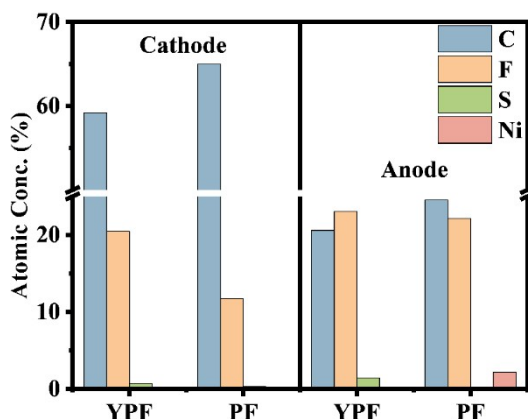


Fig. S24 Distribution of elements in NCM811 and lithium metal end of YPF and PF electrolyte after 200 cycles of 15 C.

YPF electrolyte has higher F and S elements at both the NCM811 end and the lithium metal end after circulation, which contributes to high ion conductivity and high stability EEI film formation. In addition, the lithium metal end of PF electrolyte after circulation has a high proportion of Ni elements, indicating that PF electrolyte can not inhibit the particle breakage and transition metal element escape of the positive electrode NCM811 at high magnification.

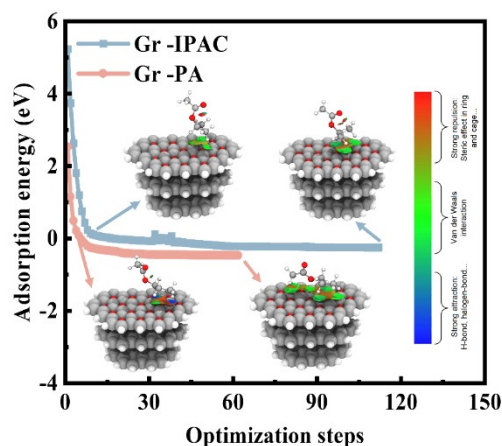


Fig. S25 Adsorption curves of IPAC and PA molecules on a graphite surface.

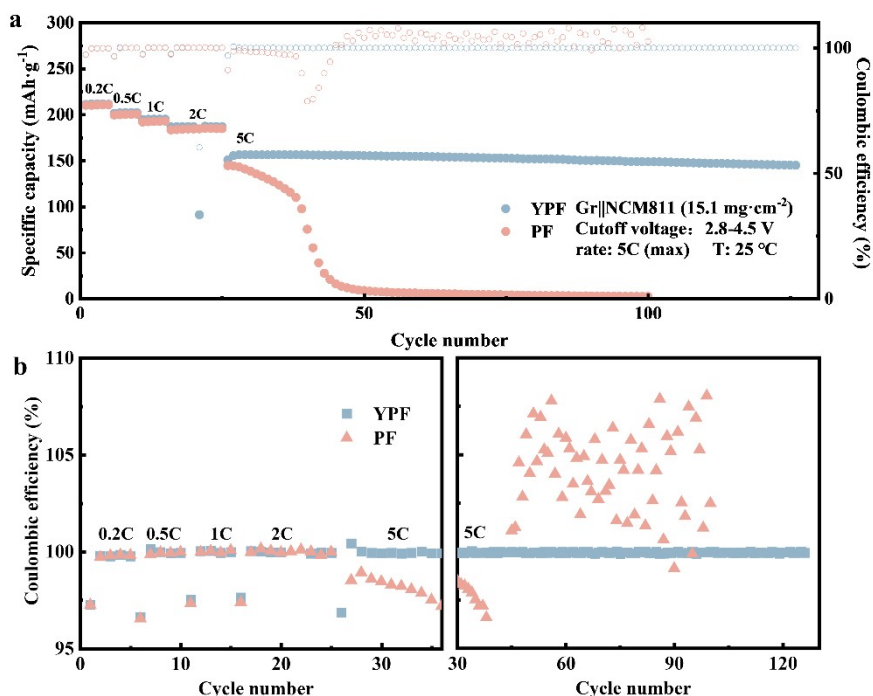


Fig. S26 Rate performance tests of different electrolytes in Gr||NCM811 cells (a) and Coulomb efficiency (b).

In the rate performance test, the capacity retention and coulombic efficiency of PF electrolyte and YPF electrolyte are similar at low rates. This is mainly because, during high-rate charging and discharging of Gr||NCM811, the speed and difficulty of intercalation/deintercalation of ions within the graphite layers become the primary limiting factors, while the desolvation energies of YPF electrolyte and PF electrolyte remain comparable. However, at high rates, YPF electrolyte significantly outperforms PF electrolyte.

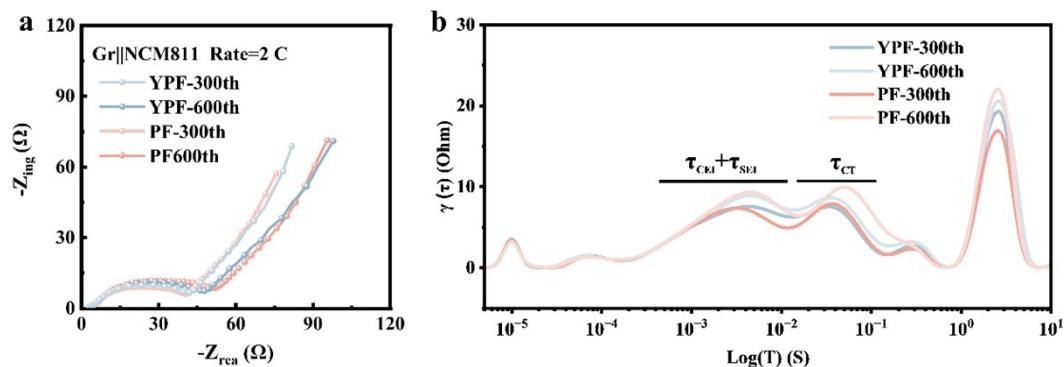


Fig. S27 The EIS curves (a) of Gr || NCM811 cells with YPF electrolyte and PF electrolyte after cycling at room temperature, as well as the DRT results (b) analyzed from the EIS curves.

EIS tests were conducted on Gr || NCM811 cells, and it was found that there was only one obvious impedance arc, making it difficult to fit a suitable curve. Through DRT analysis of EIS,¹⁵ it was found that mainly $R_{sei}+R_{cei}$ was coupled with R_{ct} .

During the 2 C cycling process, there is not much difference between the YPF electrolyte and the PF electrolyte in the short-term cycle (300 cycles), and the R_{sei} and R_{ct} of the cells with YPF electrolyte and PF electrolyte are similar. However, after 600 cycles, the R_{sei} and R_{ct} of the PF electrolyte gradually become higher than those of the YPF electrolyte.

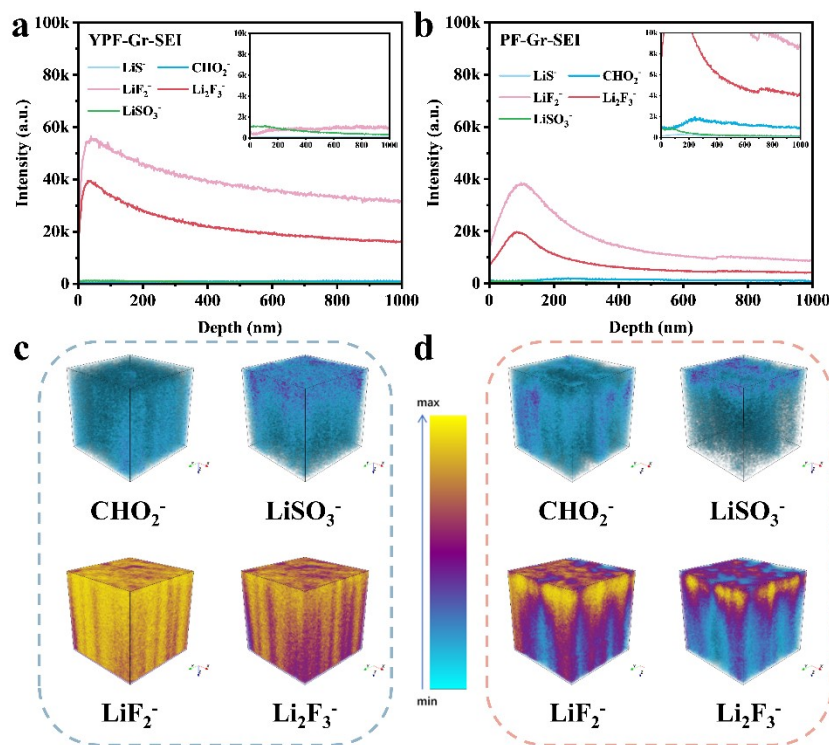


Fig. S28 After 600 cycles of Gr || NCM811 cells with different electrolytes at 4.5 V and 2 C, TOF-SIMS tests were carried out on the graphite anode side. Depth distribution diagrams of LiS^- , CHO_2^- , LiF_2^- , $Li_2F_3^-$, $LiSO_3^-$ ions and mapping images of some ion fragments (YPF electrolyte: a, c. PF electrolyte: b, d).

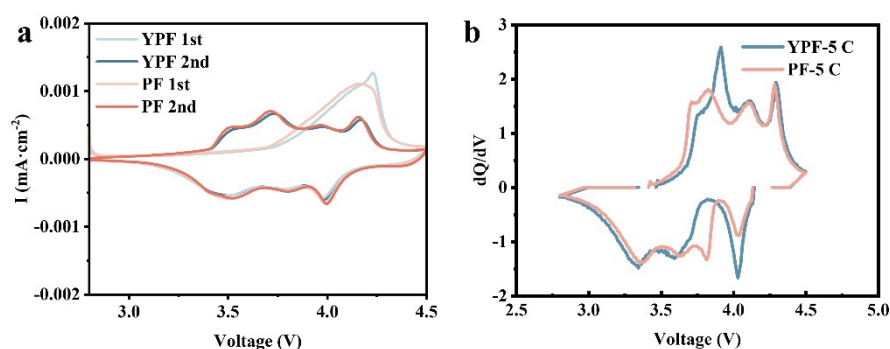


Fig. S29 The 1st and 2nd cycle CV curves of the Gr||NCM811 cells at a sweep rate of 0.1 mV/s (a). The dQ/dV curve of the Gr||NCM811 cells at 5 C (b).

The CV curves of YPF electrolyte and PF electrolyte in Gr||NCM811 cell and Li||NCM811 cell have the same trend, and YPF both have relatively delayed current peaks, which is mainly due to the enrichment of ion clusters in YPF electrolyte on the electrode surface. This results in lower lithium-ion conduction at the liquid end of the interface and stronger ion interaction to inhibit the desolvation of lithium. The dQ/dV curve shows a similar trend, but in the 5C dQ/dV curve, the sharper peaks of the YPF electrolyte represent better protection of the electrode material stability at high rates.

This indicates that the two electrolytes have similar action mechanisms in Gr||NCM811 cell and Li||NCM811 cell

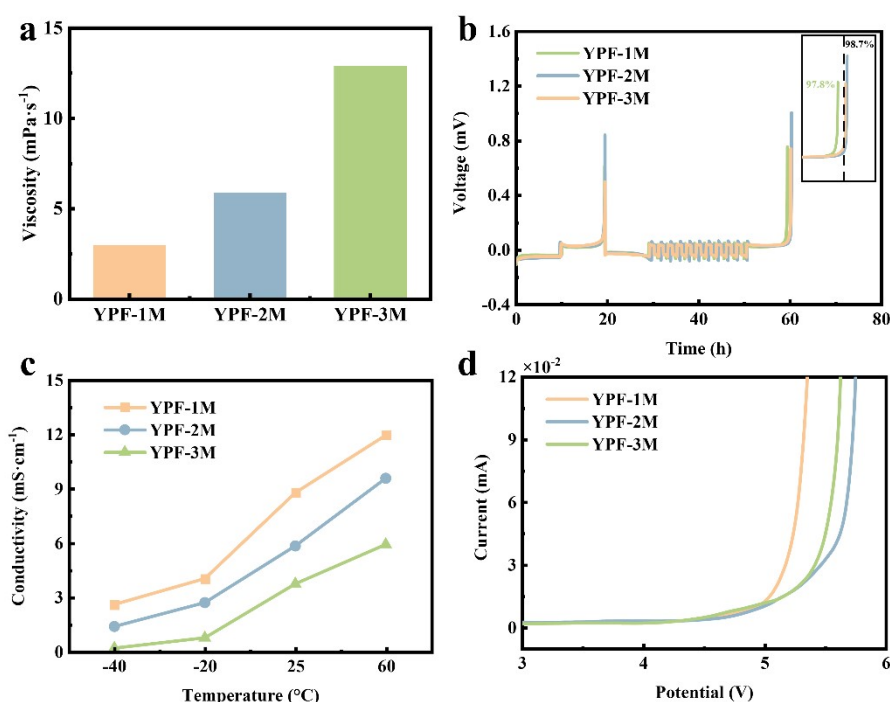


Fig. S30 Comparison of viscosity (a), conductivity (b), LSV (c), and Li||Cu (d) properties of YPF electrolyte with different concentrations.

Isopropyl acetate has the characteristic that the electrochemical window of carboxylate is not wide enough, and it needs to be configured with moderate lithium salt concentration to obtain a balanced performance. When the concentration of

lithium salt is 1M, the efficiency of the Li|Cu cells is too low, and the initial oxidation potential of the LSV test is too low. That is, the anti-oxidation-reduction performance is too poor. When the concentration of lithium salt reaches 3M, the viscosity is too high, and the conductivity at room temperature and low temperature is too low. When the electrolyte is about 2M, the properties are at a very balanced level, which is conducive to the study of the long-term circulation influence of the electrolyte and the subtle effect of the interface.

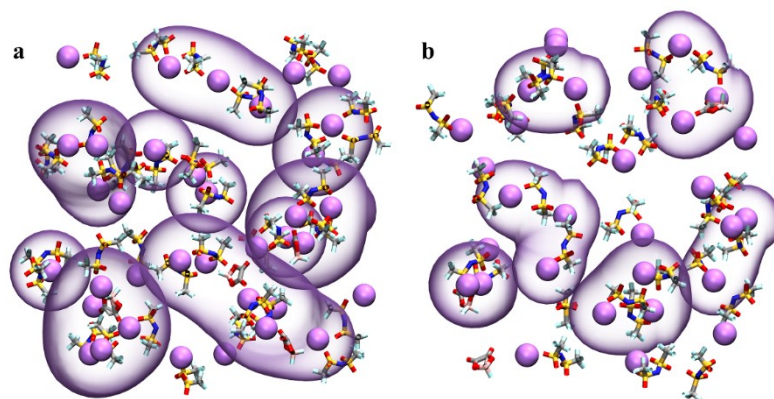


Fig. S31 MD calculated YPF electrolyte clusters (a) and PF electrolyte clusters (b).

Purple bubbles are used to classify AGG clusters, and YPF electrolyte has a significantly higher AGG ratio and larger ion clusters.

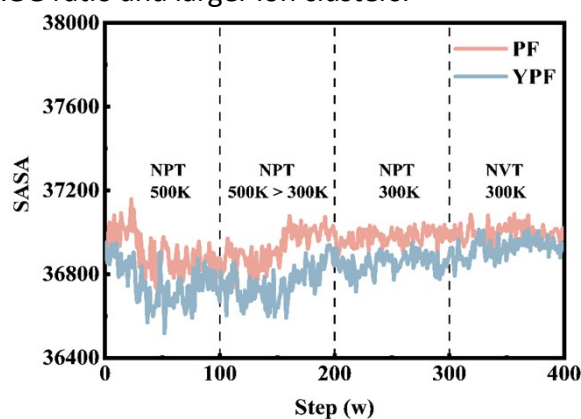


Fig. S32 SASA calculation of MD.

SASA (solvent-accessible surface area) is the molecular surface area that the solvent can contact. With lithium-ion as the centre, calculating the SASA of lithium-ion and other anions and solvents can be a good judge of the distribution uniformity of lithium ions, as well as the total surface area of lithium ions in contact with other molecules, to determine whether the electrolyte has reached an equilibrium state. PF electrolyte and YPF electrolyte fluctuate around 300K with the temperature approaching 300K. The SASA of both fluctuates in a small range. That is, the lithium ions of the electrolyte reach a stable equilibrium state in contact with other molecules.

Supporting Tables

Table S1. Disadvantages of common carboxylate electrolytes and statistics of improvement strategies

Electrolyte	Battery	Temperature range (°C)	Fast charge upper limit	The number of cycles and capacity retention rate at 25 °C	Year	Ref
LiPF ₆ EC/EMC/MA	NCM622/Li	20-40	4 C	25 °C-4C-200th-66.2%	2020	16
LiPF ₆ MP/FEC	NCM111/Gr	-40-25	10 C	25 °C-10 C-80 mAh·g ⁻¹ , -20 °C-0.5C-120th-84%	2021	17
LiPF ₆ EMC/MA	NCM622/Gr	-5	3 C	3 C-162 mAh·g ⁻¹ , -5 °C-0.5 C-100th-89.8%	2021	18
5M LiTFSI EA/DCM	Li/PI	-70-25	10	-70 °C -0.2 C-84 mAh·g ⁻¹	2019	5
LiTFSI+LiODFB EA/TMS/FEC	NCM523/Li	-40-25	10 C	-40 °C-1 C-100 mAh·g ⁻¹ , 25 °C -10 C-130 mAh·g ⁻¹ , 25 °C -1 C-200th-65%	2021	19
LiTFSI+LiODFB +LiNO ₃ MA/FEC	NCM523/Li	-40-30	0.2 C	-40 °C-0.2 C-150th-84%	2023	20
LiPF ₆ EFA/VC	LiCoO ₂ /Gr	-40-25	4 C	25 °C -1 C-400th-87.7%	2024	21
LiPF ₆ +LiODFB EA-f/FEC	NCM622/Gr	-40-25	2 C	-20 °C -C/3-300th-97% 25 °C -2 C-400th-91%	2023	22
LiFSI EDFA/FEC	NCM811/Gr	-40-45	6 C	25 °C -0.5 C-100th-80.5%	2023	23
LiPF ₆ EC/EMC/EP	NCM811/Li	-60-25	1 C	-60 °C-0.1 C-115 mAh·g ⁻¹ , 25 °C -1 C-200th~84%	2022	24
LiPF ₆ EC/EMC/PA	NCM811/Gr			25 °C -1 C-360th~89%		

Carboxylic esters are used to prepare high-performance electrolytes, with many studies tabulated. Ma et al.²⁵ found MP and MB with longer chains had better high-temperature storage for batteries, and 40% MP-containing batteries charged faster. However, carboxylic-electric-based electrolytes have safety risks due to low boiling points and high volatility, and their reactive carbonyls cause impedance and capacity decay.

Researchers proposed strategies. Zhao et al.¹⁹ got 50% capacity retention at -40 °C with a dual-salt system. Xia et al.⁵ used DCM to keep electrolyte liquid at -70 °C but it worsened high-temp stability. Fluorination can enhance oxidation resistance, like FEA, by improving cycling stability. But over-fluorination causes issues. Xia et al.²³

chose EDFA for balanced performance.

Current research focuses on the low-temperature performance of linear esters, which is lacking in high-rate and high-low-temperature studies. This paper innovatively used IPAC with a steric hindrance effect as the main solvent. It reduced interface concentration and contact. With additives, a new electrolyte was made. The study of the structure-activity relationship revealed the regulatory mechanism of the branched chain on lithium deposition and SEI film. Also, the ultra-high-rate cycling performance was studied, offering new ideas for wide-temp and fast-charging batteries.

Table S2. Statistics and comparison of advanced electrolytes and latest electrolyte strategies

Electrolyte	Battery	Temperature range (°C)	Fast charge upper limit	The number of cycles and capacity retention rate at 25 °C	Year	Ref
1.4M LiFSI DMC/EC/TTE	NCM811/Gr	-30-60	3 C	-30 °C-0.2 C-200th-85.6%, 60 °C-3 C-100th-94.9%	2020	26
2.0 M LiFSI-AN-FB	NCM811/Gr	-40-25	5 C	25 °C-5 C-500th-80%	2022	27
	LTO/Li		0.1 C	-40 °C-0.1 C-200th-91.1%		
4 M LBF in FEC/MA/TFME	LNMO/Li	-40-25	5 C	-40 °C-0.1 C-100th-93.8%, 25 °C-1 C-200th-98.34%, 25 °C-5 C-162 mAh·g ⁻¹	2022	28
LiFSI xDMC/EC/TTE	NCM811/Gr	25	4 C	25 °C-4 C-300th-92.7%	2023	29
1.6M LiFSI DMC/EC/HFE	MNC532/Gr	25	5 C	25 °C-6 C-150th-84.4%	2023	30
LiPF ₆ TFA/EMC/VC/HFA	NCM811/Gr	45	3 C	45 °C-3 C-700th-82%	2023	31
LiODFB NMFTA	LFP/Li	25-100	20 C	25 °C-200th-99.38%, 100 °C-20 C -1000th-82.79%	2024	32
0 M LiPF ₆ EC/DMC	NCM111/Gr	25	4 C	25 °C-4 C-300th-89%	2024	33
LiFSI PES/FEC	LFP/Li	25	10 C	25 °C-10 C-1000th-81.32%	2024	34
LiFSI DME/TTE	LiCoO ₂ /Gr	25	4 C	25 °C-4 C-104 mAh·g ⁻¹	2024	35
LiFSI DOL	LFP/NG	-30-25	60 C	25 °C-60 C-1000th- 60 mAh·g ⁻¹	2024	36
LiPF ₆ FEC/AN	NCM811/NG	25	20 C	25 °C-4 C-100th-170 mAh·g ⁻¹		
LiDFOB+LiNO ₃ DME/PFPN	NCM811/Li	25	3 C	25 °C-3 C-160th-74%	2024	37
Our work	NCM811/Gr	25	2 C	25 °C-2 C-1000th-85.9%	2024	/
	NCM811/Li	-60-60	20 C	25 °C-20 C-137.2 mAh·g ⁻¹ , 25 °C-15 C-200th-87%, -20 °C-1 C-200th-90.2%, -60°C-0.1 C-118mAh·g ⁻¹		

Here, we conducted a comprehensive literature survey on advanced electrolytes and summarized the formulations with outstanding performance in recent years. It is evident that electrode interface stability plays a crucial role in achieving wide

temperature tolerance, high-rate capability, and long cycling life for batteries. Historically, local high-concentration electrolyte (LHCE) design has been widely adopted, adding diluents to reduce overall viscosity while maintaining high lithium salt concentration to ensure sufficient interfacial stability. This approach has laid the foundation for achieving fast charging performance, with most electrolytes capable of sustaining long-term cycling at rates exceeding 1 C.^{27, 28, 30, 38} Additionally, additives for enhancing interfacial stability, such as fluorinated solvents, lithium salts, and LiNO_3 , have been frequently considered in electrolyte design.^{27, 28, 30, 34, 36, 37} Recently, attention has shifted to the non-negligible impact of the electric double layer (EDL) on interface film formation. For instance, Fan et al.³⁹ successfully utilized fluorinated silyl ether solvents to modulate the chemical composition of the EDL, significantly improving the cycle life of lithium-ion batteries at room temperature. Our work focuses on optimizing the composition of the EDL by employing branched-chain structures instead of straight-chain ones, thereby enhancing the high-rate cycling performance of both lithium metal and lithium-ion batteries.

Table S3. The binding energy of solvent and lithium-ion.

	E_{Li^+}	Insolvent	Compound	E_{BSSE}	$E_{Binding}$ (Hartree)	$E_{Binding}$ (eV)
Li⁺-FEC	-7.4231	-441.8621	-449.3102	0.00017	-0.0250	-0.6820
Li⁺-PA	-7.4231	-347.1965	-354.6510	0.00010	-0.0313	-0.8544
Li⁺-IPAC	-7.4231	-347.2010	-354.6561	0.00012	-0.0320	-0.8715

The binding energy error caused by the base group was corrected by the formula:

$$E_{binding} = E_{compound} - E_{Li^+} - E_{solvent} + E_{BSSE}$$

Table S4. MD calculation error comparison.

Reagent	Analog density	Actual density	Error (%)
Isopropyl acetate (IPAC)	0.871	0.872	0.1
Propyl acetate (PA)	0.880	0.888	0.9
Fluorocarbonate (FEC)	1.438	1.454	1.1
YPF electrolyte	1.263	1.268	0.4
PF electrolyte	1.265	1.272	0.5

MD calculated the density of each solvent, YPF electrolyte, and PF electrolyte compared with the actual reagent and found a minimal density difference. The choice of force field parameters is reasonable.

References

1. J. Ming, Z. Cao, Q. Li, W. Wahyudi, W. Wang, L. Cavallo, K.-J. Park, Y.-K. Sun and H. N. Alshareef, *ACS Energy Letters*, 2019, **4**, 1584-1593.
2. T. Ma, Y. Ni, Q. Wang, W. Zhang, S. Jin, S. Zheng, X. Yang, Y. Hou, Z. Tao and J. Chen, *Angewandte Chemie International Edition*, 2022, **61**, e202207927.
3. W. Zhang, Y. Lu, L. Wan, P. Zhou, Y. Xia, S. Yan, X. Chen, H. Zhou, H. Dong and K. Liu, *Nature Communications*, 2022, **13**, 2029.
4. E. Park, J. Park, K. Lee, Y. Zhao, T. Zhou, G. Park, M.-G. Jeong, M. Choi, D.-J. Yoo, H.-G. Jung, A. Coskun and J. W. Choi, *ACS Energy Letters*, 2023, **8**, 179-188.
5. X. Dong, Y. Lin, P. Li, Y. Ma, J. Huang, D. Bin, Y. Wang, Y. Qi and Y. Xia, *Angewandte Chemie International Edition*, 2019, **58**, 5623-5627.
6. H. Dou, X. Wu, M. Xu, R. Feng, Q. Ma, D. Luo, K. Zong, X. Wang and Z. Chen, *Angewandte Chemie International Edition*, 2024, **63**, e202401974.
7. X. Zhou, Q. Zhang, Z. Zhu, Y. Cai, H. Li and F. Li, *Angewandte Chemie International Edition*, 2022, **61**, e202205045.
8. N. Yao, X. Chen, Z.-H. Fu and Q. Zhang, *Chemical Reviews*, 2022, **122**, 10970-11021.
9. H.-R. Cheng, Z. Ma, Y.-J. Guo, C.-S. Sun, Q. Li and J. Ming, *Journal of Electrochemistry*, 2022, **28**, 2219012.
10. C. M. Efav, Q. Wu, N. Gao, Y. Zhang, H. Zhu, K. Gering, M. F. Hurley, H. Xiong, E. Hu, X. Cao, W. Xu, J.-G. Zhang, E. J. Dufek, J. Xiao, X.-Q. Yang, J. Liu, Y. Qi and B. Li, *Nature Materials*, 2023, **22**, 1531-1539.
11. T. Li, X.-Q. Zhang, N. Yao, Y.-X. Yao, L.-P. Hou, X. Chen, M.-Y. Zhou, J.-Q. Huang and Q. Zhang, *Angewandte Chemie International Edition*, 2021, **60**, 22683-22687.
12. M. Qin, M. Liu, Z. Zeng, Q. Wu, Y. Wu, H. Zhang, S. Lei, S. Cheng and J. Xie, *Advanced Energy Materials*, 2022, **12**, 2201801.
13. Z. Yu, N. P. Balsara, O. Borodin, A. A. Gewirth, N. T. Hahn, E. J. Maginn, K. A. Persson, V. Srinivasan, M. F. Toney, K. Xu, K. R. Zavadil, L. A. Curtiss and L. Cheng, *ACS Energy Letters*, 2022, **7**, 461-470.
14. W. Yuankun, L. Zhiming, H. Yunpeng, H. Zhimeng, Z. Qiu, N. Youxuan, L. Yong, Y. Zhenhua, Z. Kai, Z. Qing, L. Fujun, C. Jun, A.-M. Li, O. Borodin, T. P. Pollard, W. Zhang, N. Zhang, S. Tan, F. Chen, C. Jayawardana, B. L. Lucht, E. Hu, X.-Q. Yang and C. Wang, *CHEMICAL SOCIETY REVIEWS*, 2023, **16**, 2713-2763.
15. R. Xu, A. Hu, Z. Wang, K. Chen, J. Chen, W. Xu, G. Wu, F. Li, J. Wang and J. Long, *Journal of Energy Chemistry*, 2025, **105**, 35-43.
16. X. Wu, T. Liu, Y. Bai, X. Feng, M. M. Rahman, C.-J. Sun, F. Lin, K. Zhao and Z. Du, *Electrochimica Acta*, 2020, **353**, 136453.
17. Y.-G. Cho, M. Li, J. Holoubek, W. Li, Y. Yin, Y. S. Meng and Z. Chen, *ACS Energy Letters*, 2021, **6**, 2016-2023.
18. Y. Zou, Z. Cao, J. Zhang, W. Wahyudi, Y. Wu, G. Liu, Q. Li, H. Cheng, D. Zhang, G.-T. Park, L. Cavallo, T. D. Anthopoulos, L. Wang, Y.-K. Sun and J. Ming, *Advanced Materials*, 2021, **33**, 2102964.
19. S. Lin, H. Hua, P. Lai and J. Zhao, *Advanced Energy Materials*, 2021, **11**, 2101775.
20. X. Meng, J. Qin, Y. Liu, Z. Liu, Y. Zhao, Z. Song and H. Zhan, *Chemical Engineering Journal*, 2023, **465**, 142913.

21. L. Luo, K. Chen, R. Cao, H. Chen, M. Xia, A. Zhao, X. Chen, W. Chen, Z. Chen, Y. Fang and Y. Cao, *Energy Storage Materials*, 2024, **70**, 103438.
22. D.-J. Yoo, Q. Liu, O. Cohen, M. Kim, K. A. Persson and Z. Zhang, *Advanced Energy Materials*, 2023, **13**, 2204182.
23. Y. Mo, G. Liu, Y. Yin, M. Tao, J. Chen, Y. Peng, Y. Wang, Y. Yang, C. Wang, X. Dong and Y. Xia, *Advanced Energy Materials*, 2023, **13**, 2301285.
24. X. Deng, S. Zhang, C. Chen, Q. Lan, G. Yang, T. Feng, H. Zhou, H. Wang, Z. Xu and M. Wu, *Electrochimica Acta*, 2022, **415**, 140268.
25. X. Ma, R. S. Arumugam, L. Ma, E. Logan, E. Tonita, J. Xia, R. Petibon, S. Kohn and J. R. Dahn, *Journal of The Electrochemical Society*, 2017, **164**, A3556.
26. , !!! INVALID CITATION !!! .
27. S. Lei, Z. Zeng, M. Liu, H. Zhang, S. Cheng and J. Xie, *Nano Energy*, 2022, **98**, 107265.
28. T. Feng, G. Yang, S. Zhang, Z. Xu, H. Zhou and M. Wu, *Chemical Engineering Journal*, 2022, **433**, 134138.
29. D. J. Kautz, X. Cao, P. Gao, B. E. Matthews, Y. Xu, K. S. Han, F. Omenya, M. H. Engelhard, H. Jia, C. Wang, J.-G. Zhang and W. Xu, *Advanced Energy Materials*, 2023, **13**, 2301199.
30. X. Yue, J. Zhang, Y. Dong, Y. Chen, Z. Shi, X. Xu, X. Li and Z. Liang, *Angewandte Chemie International Edition*, 2023, **62**, e202302285.
31. K. An, D. Kim, Y. H. T. Tran, D. T. T. Vu, S. J. Park, J. Heo, Y. J. Lee and S.-W. Song, *Advanced Functional Materials*, 2024, **34**, 2311782.
32. M. Fang, X. Yue, Y. Dong, Y. Chen and Z. Liang, *Joule*, 2024, **8**, 91-103.
33. C. Li, Z. Liang, L. Wang, D. Cao, Y.-C. Yin, D. Zuo, J. Chang, J. Wang, K. Liu, X. Li, G. Luo, Y. Deng and J. Wan, *ACS Energy Letters*, 2024, **9**, 1295-1304.
34. J. Wang, L. Xie, W. Wu, Y. Liang, M. Cao, C. Gao, Y. Bo, J. Zhang and J. Zhang, *Energy & Environmental Science*, 2024, DOI: 10.1039/D4EE00391H.
35. Y. Wang, Y. Ji, Z.-W. Yin, T. Sheng, A. Cao, W. Zhao, Y. Huang, J.-T. Li, F. Pan and L. Yang, *Advanced Functional Materials*, 2024, **34**, 2401515.
36. C. Sun, X. Ji, S. Weng, R. Li, X. Huang, C. Zhu, X. Xiao, T. Deng, L. Fan, L. Chen, X. Wang, C. Wang and X. Fan, *Advanced Materials*, 2022, **34**, 2206020.
37. T. Yang, L. Li, J. Zou, Y. Yao, Q. Zhang, Z. Jiang and Y. Li, *Advanced Functional Materials*, 2024, **n/a**, 2404945.
38. X. Zhang, L. Zou, Y. Xu, X. Cao, M. H. Engelhard, B. E. Matthews, L. Zhong, H. Wu, H. Jia, X. Ren, P. Gao, Z. Chen, Y. Qin, C. Kompella, B. W. Arey, J. Li, D. Wang, C. Wang, J.-G. Zhang and W. Xu, *Advanced Energy Materials*, 2020, **10**, 2000368.
39. L. Chen, H. Zhang, R. Li, S. Zhang, T. Zhou, B. Ma, C. Zhu, X. Xiao, T. Deng, L. Chen and X. Fan, *Chem*, 2024, **10**, 1196-1212.